Constitutive model for fibre reinforced composites with progressive damage based on the spectral decomposition of material stiffness tensor

Rade Vignjevic [a],[*], Nenad Djordjevic [a], Agata Galka [a], Gareth Appleby-Thomas [b], Kevin Hughes [a]

[a] *Brunel University London, Centre for Assessment of Structures and Materials Under Extreme Conditions, Mechanical and Aerospace Engineering, Cambridge CB21 6AL, UK*
[b] *Cranfield University, Defence Academy of the United Kingdom, Centre for Defence Engineering, Shrivenham SN6 8LA, UK*

A B S T R A C T

Complex nature of the fibre reinforced composites, their non-homogeneity and anisotropy make their modelling a challenging task. Although the linear – elastic behaviour of the composites is well understood, there is still a significant uncertainty regarding prediction of damage initiation, damage evolution and material failure especially for a general loading case characterised with triaxial state of stress or strain. Consequently, simplifying assumptions are often unavoidable in development of constitutive models capable of accurately predicting damage. The approach used in this work uses decomposition of the strain energy based on spectral decomposition of the material stiffness tensor and an assumption that each strain energy component represent free energy for a characteristic deformation mode. The criteria for damage initiation are based on an assumption that the damage corresponding to a deformation mode is triggered when the strain energy for that mode exceeds a specified critical limit. In the proposed model the deformation modes are not interacting at continuum scale due to orthogonality of the eigenvectors, i.e. the stiffness tensor symmetry. Damage and its evolution are modelled by reduction of the principal material stiffness based on the effective stress concept and the hypothesis of strain energy equivalence. The constitutive model was implemented into Lawrence Livermore National Laboratory (LLNL) Dyna3d explicit hydrocode and coupled with a vector shock Equation of State. The modelling approach was verified and validated in a series of single element tests, plate impact test and high velocity impact of hard projectile impact on an aerospace grade carbon fibre reinforced plastic. The model accurately predicted material response to impact loading including the test cases characterised by presence of shock waves, e.g. the plate impact test. It was also demonstrated that the model was capable of predicting damage and delamination development in the simulation of the high velocity impact tests, where the numerical results were within 5% of the post impact experimental measurements.

1. Introduction

Damage in a material depends on its life cycle starting with design process, through manufacturing and exploitation. Design and manufacturing are complex processes dependent on the large number of parameters, which determine the final material quality. A good example are residual stresses between the fibres and matrix due to different thermal expansion during curing process. Design and manufacturing of composites, although important for the material quality, lay beyond the scope of this work. This work focuses solely on the in-service behaviour of composites.

Extent and character of damage in composites depends on their architecture, properties of constituents, loading rates and load types. Based on the loading rate/impact velocity, one can distinguish low velocity (LVI) and high velocity impacts (HVI), although some authors also identify hypervelocity and ballistic impacts [1,2]. A low velocity impact is typically characterised by impact velocities up to about 50 m/s [3]. In a LVI structures respond globally where the impact event time scale allows for impact energy transfer from the impact zone into the global deformation modes of the structure. LVI are typically modelled as quasi-static events, where inertial and strain rate effects are neglected. Typically, LVI does not lead to instantaneous collapse of the structure but to reduction of stiffness, strength and reduction in fatigue life combined with damage with low detectability. The commonly used example of low

---

velocity impact is tool dropping, which can lead to delamination which is difficult to detect because it forms below material surface with no visible trace. However, it can cause significant strength and stiffness reduction and compromise the safety of the structure. Composite behaviour under LVI has been widely studied to provide the insight into damage mechanisms related to different impact stages [4].

Investigation of damage in composites under **high velocity impact** (HVI) is far more complicated because of the impact short time scale; the difficulties arise in experiment design especially in terms of observation of damage effects [1]. Understanding the HVI behaviour of composite materials is critically important for defence and aerospace sectors, where HVI such as debris and hailstone impacts, bird strike, fragment and projectile impacts are of safety critical. Bird strike and debris impact can lead to catastrophic structural failures and consequently to fatal accidents – one example is Concorde accident in Paris in 2000. In this incident debris from the runway hit the aircraft fuel tank leading to fire.

Although this work concentrates on aerospace application of composites it should be noted that it could be of interest to other industries including the wind energy, automotive, military and defence. In case of wind turbines, the blades can be damaged and destroyed by hailstones during heavy storms. Important aspect of HVI, that is not of high importance in low velocity impact, is generation of stress and shock waves in the material which propagate at high speeds.

The presence of at least two constituents/phases in composite materials also implies presence of an interface between the constituents with the interface properties different from properties of the constituents. Consequently, damage mechanisms that evolve in the material can be related to either of the constituents/phases and/or their interface as described in [6]. These mechanisms are: matrix microcracking, fibre breakage, fibre microbuckling, interfacial debonding and delamination (interlaminar cracking).

In the development of the proposed material model the following intralamina damage mechanisms were considered: matrix microcracking, fibre breakage and interfacial debonding. These types of damage were considered through mesoscale modelling of the composite where stiffness and strength properties of the matrix and fibres were varied in order to represent specific extent of the corresponding physical damage. The damage related to the fibre matrix interface was represented by varying fibre matrix contact properties in the models.

It is important to note that the energy-based nature of the model allows for additional damage mechanisms to be added.

The approach adopted for the model formulation has very limited commonality with the majority of the models for modelling of progressive damage and failure in composites available in public domain literature. Consequently, the number of references used in this work is limited (23 relevant publications only).

The paper is organized as follows: Section 2, provides description of the thermodynamic framework used for the model development and Helmholtz free energy decomposition based on spectral decomposition of the material stiffness tensor. The section concludes with development of constitutive relation for a single mode of deformation. Section 3 describes mesoscale modelling of unidirectional composite used to verify the basic assumptions used in the model development and the material model characterisation. Description of the model verification and validation based on the modelling of the plate impact and steel projectile impact experiments is given in Section 4. Conclusions related to the outcome of this work are given in Section 5.

2. Model formulation

This section starts with a description of the main assumptions used in the model development. The proposed model is a continuum scale model inspired by the work of Schreyer and Zuo [7,8] who used spectral decomposition in definition of material failure criteria. Fibre Reinforced Composites, in general, are anisotropic material with linear elastic behaviour described by the generalised Hooke's Law given in the Voigt

notation in symbolic tensor and index form as [9]:

$$\boldsymbol{\sigma} = \boldsymbol{C}\,\boldsymbol{\varepsilon} \quad \sigma_\alpha = C_{\alpha\beta}\varepsilon_\beta \tag{1}$$

where: $\boldsymbol{\sigma}$ and $\boldsymbol{\varepsilon}$ are stress and strain vectors respectively and $\boldsymbol{C}$ is symmetric second order tensor representing material stiffness.

The above equations for transversely isotropic material in matrix form can be written as:

$$\begin{bmatrix} \sigma_1 \\ \sigma_2 \\ \sigma_3 \\ \sqrt{2}\sigma_4 \\ \sqrt{2}\sigma_5 \\ \sqrt{2}\sigma_6 \end{bmatrix} = \begin{bmatrix} C_{11} & C_{12} & C_{12} & 0 & 0 & 0 \\ C_{12} & C_{22} & C_{23} & 0 & 0 & 0 \\ C_{12} & C_{23} & C_{22} & 0 & 0 & 0 \\ 0 & 0 & 0 & C_{22}-C_{23} & 0 & 0 \\ 0 & 0 & 0 & 0 & 2C_{66} & 0 \\ 0 & 0 & 0 & 0 & 0 & 2C_{66} \end{bmatrix} \cdot \begin{bmatrix} \varepsilon_1 \\ \varepsilon_2 \\ \varepsilon_3 \\ \sqrt{2}\varepsilon_4 \\ \sqrt{2}\varepsilon_5 \\ \sqrt{2}\varepsilon_6 \end{bmatrix} \tag{2}$$

where the factors $\sqrt{2}$ ensure the standard tensor operations apply.

The diagonalization of the stiffness tensor given in Eq. (2) leads to identification of the six eigenvalues and corresponding eigenvectors. Therefore, the stiffness tensor $\boldsymbol{C}$ can be spectrally decomposed and represented as:

$$\boldsymbol{C} = \sum_{i=I}^{VI} \lambda^i \boldsymbol{P}^i \quad \boldsymbol{P}^i = \boldsymbol{v}^i \otimes \boldsymbol{v}^i \tag{3}$$

where: λ^i are eigenvalues, $\boldsymbol{v}^i$ are unit eigenvectors, $\boldsymbol{P}^i$, $i = I, II, ..., VI$ are projection operator tensors. The roman numbers used as the superscripts to indicate the modes should not be treated as the exponents. Eigenvalues of the stiffness tensor can be considered as the material principal stiffnesses, their explicit expressions for transversely isotropic materials can be found, for instance, in [8–12]. The unit eigenvectors $\boldsymbol{v}^i$ define the material bases and are calculated as:

$$\boldsymbol{v}^I = \frac{1}{\sqrt{2+\alpha^2}}\begin{bmatrix} \alpha & 1 & 1 & 0 & 0 & 0 \end{bmatrix}^T \quad \alpha = \frac{2C_{12}}{\lambda^I - C_{11}} \tag{4}$$

$$\boldsymbol{v}^{III} = \frac{1}{\sqrt{2+\beta^2}}\begin{bmatrix} \beta & 1 & 1 & 0 & 0 & 0 \end{bmatrix}^T \quad \beta = \frac{2C_{12}}{\lambda^{III} - C_{11}}$$

$$\boldsymbol{v}^{II} = \frac{1}{\sqrt{2}}\begin{bmatrix} 0 & -1 & 1 & 0 & 0 & 0 \end{bmatrix}^T \quad \boldsymbol{v}^{IV} = \begin{bmatrix} 0 & 0 & 0 & 1 & 0 & 0 \end{bmatrix}^T$$

$$\boldsymbol{v}^V = \begin{bmatrix} 0 & 0 & 0 & 0 & 1 & 0 \end{bmatrix}^T \quad \boldsymbol{v}^{VI} = \begin{bmatrix} 0 & 0 & 0 & 0 & 0 & 1 \end{bmatrix}^T$$

One of the main assumptions in the formulation of the model was that the eigenvectors were invariant (not varying with material deformation). This assumption was validated for a unidirectional composite through mesoscale modelling presented in Section 3.

Spectral decomposition of the stiffness tensor allows for constitutive relationship to be defined as:

$$\boldsymbol{\sigma} = \boldsymbol{C} \cdot \boldsymbol{\varepsilon} = \sum_{i=I}^{VI} \lambda^i \boldsymbol{P}^i \cdot \boldsymbol{\varepsilon} = \sum_{i=I}^{VI} \lambda^i \boldsymbol{\varepsilon}^i = \sum_{i=I}^{VI} \boldsymbol{\sigma}^i \quad \boldsymbol{\varepsilon}^i = \boldsymbol{P}^i \cdot \boldsymbol{\varepsilon} \tag{5}$$

where $\boldsymbol{\varepsilon}^i$ and $\boldsymbol{\sigma}^i$ are the modal strain and stress components respectively, i.e. the strain component collinear with the ith eigenvector. Note, the modal stresses are defined in terms of the modal strain components and the material stiffness eigenvalues and corresponding projection operators as:

$$\boldsymbol{\sigma}^i = \lambda^i \boldsymbol{\varepsilon}^i \quad \boldsymbol{\sigma}^i = \boldsymbol{P}^i \cdot \boldsymbol{\sigma} \tag{6}$$

Damage was assumed to be mode-specific and was included in the constitutive equation using the effective stress concept and the strain energy equivalence hypothesis, according to which the damaged material stiffness $\boldsymbol{C}(\mathscr{D})$ is defined as:

$$\boldsymbol{C}(\mathscr{D}) = (\boldsymbol{I} - \mathscr{D})^T \cdot \boldsymbol{C}_0 (\boldsymbol{I} - \mathscr{D}) \tag{7}$$

where second order damage tensor $\mathscr{D}$ is diagonal, $\boldsymbol{I} = \delta_{ij}$ is identity

tensor and $\boldsymbol{C}_0$ is second order stiffness tensor of the virgin material (material with no damage). Note, stiffness of the damaged material $\boldsymbol{C}(\mathscr{D})$ reduces with increase of damage. Based on the assumption that damage is mode specific, i.e. damage modes are uncoupled, Eq. (7) simplifies to:

$$C(d^i) = \sum_{i=I}^{VI} (1 - d^i)^2 \lambda_0^i \boldsymbol{P}^i \tag{8}$$

where d^i and λ_0^i are a scalar damage variables and eigenvalues of the virgin/undamaged stiffness tensor. Consequently, the principal stiffness of a damaged material λ_d^i can be defined as:

$$\lambda_d^i = (1 - d^i)^2 \lambda_0^i \tag{9}$$

2.1. Helmholtz free energy decomposition

The material model was developed in the framework of irreversible thermodynamics as in [13,22]. Helmholtz free energy, given by Eq. (10), comprising the strain energy and the damage associated energy was used as thermodynamic potential:

$$\Psi = W + \sum_i H_i \tag{10}$$

where W is strain energy (a measure of elastic strain energy stored in the material that can be recovered in unloading) and H_i are damage mode associated potentials. The damage potentials define the non-recoverable part of free energy associated with damage (irreversible) processes in the material. They allow for modelling of damage evolution, i.e. the damage hardening/softening of the material. Associative damage flow rule was adopted in the model.

Elastic strain energy is defined by:

$$W(\boldsymbol{\varepsilon}, d^i) = \frac{1}{2} \boldsymbol{\varepsilon} \cdot \boldsymbol{C}(\mathscr{D}) \boldsymbol{\varepsilon} \tag{11}$$

Application of the spectral decomposition, defined in Eq. (3), leads to definition of the strain energy as a sum of the modal strain energies W^i:

$$W(\boldsymbol{\varepsilon}) = \frac{1}{2} \boldsymbol{\varepsilon} \cdot \boldsymbol{C} \boldsymbol{\varepsilon} = \frac{1}{2} \boldsymbol{\varepsilon} \cdot \left(\sum_{i=I}^{VI} \lambda^i \boldsymbol{P}^i \right) \boldsymbol{\varepsilon} = \frac{1}{2} \sum_{i=I}^{VI} \lambda^i \boldsymbol{\varepsilon} \cdot \boldsymbol{P}^i \boldsymbol{\varepsilon} = \frac{1}{2} \sum_{i=I}^{VI} \lambda^i \boldsymbol{\varepsilon}^i \cdot \boldsymbol{\varepsilon}^i = \sum_{i=I}^{VI} W^i \tag{12}$$

The strain energy equivalence hypothesis leads to definition of strain energy for a damaged material as:

$$W(\boldsymbol{\varepsilon}, d^i) = \frac{1}{2} \sum_{i=I}^{VI} (1 - d^i)^2 \lambda_0^i (\boldsymbol{\varepsilon}^i)^2 \tag{13}$$

where: $(\boldsymbol{\varepsilon}^i)^2 = \boldsymbol{\varepsilon}^i \cdot \boldsymbol{\varepsilon}^i$ and $\boldsymbol{\varepsilon}^i = \boldsymbol{P}^i \cdot \boldsymbol{\varepsilon}$.

Consequently, the damage potential is a quadratic function of damage evolution variable h^i [7]. Damage is assumed to be mode specific, therefore damage evolution is also mode specific and can be expressed as:

$$H^i(h^i) = \frac{1}{2} \kappa^i (h^i)^2 \tag{14}$$

where κ^i is modal damage evolution parameter and h^i is modal damage evolution variable. Both damage and damage hardening variables are dimensionless, which implies that the material constant κ^i has the unit of energy.

Making use of equations for strain energy Eq. (13) and damage evolution associated energy Eq. (14), the final form of Helmholtz free energy potential is:

$$\Psi(\boldsymbol{\varepsilon}, d^i, h^i) = \frac{1}{2} \sum_{i=I}^{VI} (1 - d^i)^2 \lambda_0^i (\boldsymbol{\varepsilon}^i)^2 + \frac{1}{2} \sum_{i=I}^{VI} \kappa^i (h^i)^2$$

$$= \frac{1}{2} \sum_{i=I}^{VI} \left((1 - d^i)^2 \lambda_0^i (\boldsymbol{\varepsilon}^i)^2 + \kappa^i (h^i)^2 \right) = \sum_{i=I}^{VI} \Psi_i \tag{15}$$

The above equation clearly shows that Helmholtz free energy can be divided into components corresponding to the non-interacting damage modes. The model is derived with respect to the eigenvector basis which significantly simplifies the model formulation. Further, this allows for further development of the model to be described by presenting formulation of the model for a single deformation mode.

2.2. Constitutive equations for single mode

The modal Helmholtz free energy is defined by Eq. (16) as:

$$\Psi^i(\boldsymbol{\varepsilon}, d^i, h^i) = \frac{1}{2} (1 - d^i)^2 \lambda_0^i (\boldsymbol{\varepsilon}^i)^2 + \frac{1}{2} \kappa^i (h^i)^2 \tag{16}$$

The rate of change of the modal Helmholtz free energy based on the chain rule is:

$$\dot{\Psi}^i(\boldsymbol{\varepsilon}, d^i, h^i) = \frac{\partial \Psi^i}{\partial \boldsymbol{\varepsilon}^i} \dot{\boldsymbol{\varepsilon}}^i + \frac{\partial \Psi^i}{\partial d^i} \dot{d}^i + \frac{\partial \Psi^i}{\partial h^i} \dot{h}^i \tag{17}$$

Conjugate thermodynamic forces and flow rates are identified in Eq. (17). The first term in Eq. (17) represents the rate of change of the elastic (recoverable) strain energy. Consequently, the energy dissipation rate is:

$$\dot{\Upsilon}^i(\boldsymbol{\varepsilon}^i, d^i, h^i) = \frac{\partial \Psi^i}{\partial \boldsymbol{\varepsilon}^i} \dot{\boldsymbol{\varepsilon}}^i - \dot{\Psi}^i = -\frac{\partial \Psi^i}{\partial d^i} \dot{d}^i - \frac{\partial \Psi^i}{\partial h^i} \dot{h}^i \tag{18}$$

The force y_d^i conjugate to damage variable d^i and the force y_h^i conjugate to damage evolution variable h^i are defined, respectively, as:

$$y_d^i = -\frac{\partial \Psi^i}{\partial d^i} = (1 - d^i) \lambda_0^i (\boldsymbol{\varepsilon}^i)^2 \quad y_h^i = -\frac{\partial \Psi^i}{\partial h^i} = -\kappa^i h^i \tag{19}$$

Following [13], we assumed that the damage potential $\Phi^i(y_d^i, y_h^i)$, that defines failure onset and damage evolution, is a linear function of conjugate forces, i.e.

$$\Phi^i(y_d^i, y_h^i) \equiv y_d^i - (y_h^i + \omega_0^i) \leqslant 0 \tag{20}$$

where ω_0^i is the energy threshold for the damage initiation in the ith mode. Negative value of the damage potential represents thermodynamic states of the material when damage does not evolve and the damaged material is behaving as elastic with reduced stiffness. According to the associative damage flow rule damage evolution occurs when the damage potential is equal to zero. Damage potential cannot have value larger than zero, in other words the material strain energy cannot exceed its limit defined by the initial energy limit ω_0^i or the energy limit of damage hardened material $(y_h^i + \omega_0^i)$. Damage and damage evolution variables can be determined from Eq. (20), the consistency condition and the maximum entropy production (maximum dissipation) principle. The energy dissipation rate, defined by Eq. (18), combined with the constraint for associative damage evolution $\Phi^i(y_d^i, y_h^i) = 0$ is maximised using Lagrange multiplier $\dot{\Lambda}^i$ in the functionals L^i:

$$L^i = -\dot{\Upsilon}^i + \dot{\Lambda}^i \Phi^i = \frac{\partial \Psi^i}{\partial d^i} \dot{d}^i + \frac{\partial \Psi^i}{\partial h^i} \dot{h}^i + \dot{\Lambda}^i \Phi^i = y_d^i \dot{d}^i + y_h^i \dot{h}^i + \dot{\Lambda}^i \Phi^i \tag{21}$$

Consequently, damage and damage evolution variables are obtained as:

$$\frac{\partial L^i}{\partial y_d^i} = 0 \quad \Rightarrow \quad \dot{d}^i = \dot{\Lambda}^i \frac{\partial \Phi^i}{\partial y_d^i} = \dot{\Lambda}^i \quad \frac{\partial L^i}{\partial y_h^i} = 0 \quad \Rightarrow \quad \dot{h}^i = \dot{\Lambda}^i \frac{\partial \Phi^i}{\partial y_h^i} = -\dot{\Lambda}^i = -\dot{d}^i \tag{22}$$

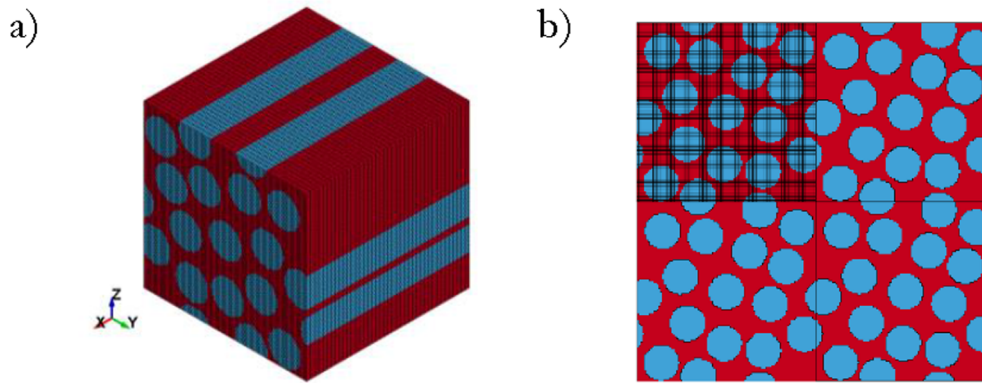Kuhn-Tucker conditions for damage evolution allow for damage

Fig. 1. Unidirectional material model representative volume element: a) isometric view, b) periodic RVE.

increase during loading of the material and do not allow for reduction of damage (material healing):

$$\dot{\Lambda}^i = \dot{d}^i \geqslant 0 \quad \Phi^i \leqslant 0 \quad \dot{\Lambda}^i \Phi^i = 0 \tag{23}$$

To ensure that during damage evolution material does not violate Eq. (20), the consistency condition must be satisfied. i.e. both the damage potential and its time derivative have to be equal to zero. This is postulated as:

$$\Phi^i\left(y_d^i, y_h^i\right) = 0 \quad \wedge \quad \dot{\Phi}^i\left(\dot{y}_d^i, \dot{y}_h^i\right) \equiv \dot{y}_d^i - \dot{y}_h^i = 0 \tag{24}$$

The rate of change of the forces conjugate to damage and damage evolution variables are given by Eq. (25):

$$\dot{y}_d^i\left(\boldsymbol{\varepsilon}^i, d^i\right) = \frac{\partial y_d^i}{\partial d^i}\dot{d}_i + \frac{\partial y_d^i}{\partial \boldsymbol{\varepsilon}^i}\dot{\boldsymbol{\varepsilon}}^i = -\lambda_0^i\left(\boldsymbol{\varepsilon}^i\right)^2\dot{d}^i + 2\left(1-d^i\right)\lambda_0^i\boldsymbol{\varepsilon}^i : \dot{\boldsymbol{\varepsilon}}^i$$

$$\dot{y}_h^i\left(h^i\right) = \frac{\partial y_h^i}{\partial h^i}\dot{h}^i = -\kappa^i \dot{h}^i = \kappa^i \dot{\Lambda}^i = \kappa^i \dot{d}^i \tag{25}$$

Substitution of Eq. (25) into Eq. (24) yields:

$$\frac{1}{\left(1-d^i\right)}\dot{d}^i = \frac{2\lambda_0^i\boldsymbol{\varepsilon}^i}{\kappa^i + \lambda_0^i\left(\boldsymbol{\varepsilon}^i\right)^2}\dot{\boldsymbol{\varepsilon}}^i \tag{26}$$

where $\left(\boldsymbol{\varepsilon}^i\right)^2$ was defined in Eq. (13). Integration of this equation, given in Appendix A-1, leads to the analytical solution for the damage variable and corresponding integration constant C^i for the ith damage mode as:

$$d^i = 1 - \frac{1}{\left(\kappa^i + \lambda_0^i\left(\boldsymbol{\varepsilon}^i\right)^2\right)C^i} \quad C^i = \frac{1}{\omega_0^i + \kappa^i} \tag{27}$$

Finally, using Eq. (27), damage variable for each damage mode can be defined as:

$$d^i = \frac{\lambda_0^i\left(\boldsymbol{\varepsilon}^i\right)^2 - \omega_0^i}{\lambda_0^i\left(\boldsymbol{\varepsilon}^i\right)^2 + \kappa^i} \tag{28}$$

2.3. Deformation eigenmodes for transversely isotropic material

For a transversely isotropic material, the modal strain vector is:

$$\boldsymbol{\varepsilon}^i = \boldsymbol{P}^i \cdot \boldsymbol{\varepsilon} = \left(\boldsymbol{v}^i \otimes \boldsymbol{v}^i\right) \cdot \boldsymbol{\varepsilon} = \left(\boldsymbol{v}^i \cdot \boldsymbol{\varepsilon}\right)\boldsymbol{v}^i \tag{29}$$

It can be demonstrated that the single contraction of a modal strain vector with itself is:

$$\bar{\boldsymbol{\varepsilon}}^{i\,2} = \left(\boldsymbol{v}^i \cdot \boldsymbol{\varepsilon}\right)\boldsymbol{v}^i \cdot \left(\boldsymbol{v}^i \cdot \boldsymbol{\varepsilon}\right)\boldsymbol{v}^i = \left(\boldsymbol{v}^i \cdot \boldsymbol{\varepsilon}\right)^2\boldsymbol{v}^i \cdot \boldsymbol{v}^i = \left(\boldsymbol{v}^i \cdot \boldsymbol{\varepsilon}\right)^2 = \left(\varepsilon^i\right)^2 \tag{30}$$

where the magnitude of the modal strain vector is: $\varepsilon^i = \boldsymbol{v}^i \cdot \boldsymbol{\varepsilon}$. The explicit solutions for the modal decomposition of the total strain vector are given below in terms of the strain components with respect to the material coordinate system:

$$\left(\bar{\varepsilon}^I\right)^2 = \left(\varepsilon^I\right)^2 = \frac{1}{2+\alpha^2}(\alpha\varepsilon_1 + \varepsilon_2 + \varepsilon_3)^2 \quad \left(\bar{\boldsymbol{\varepsilon}}^{IV}\right)^2 = \left(\varepsilon^{IV}\right)^2 = 2\varepsilon_4^2$$

$$\left(\bar{\varepsilon}^{II}\right)^2 = \left(\varepsilon^{II}\right)^2 = \frac{1}{2}(\varepsilon_2 - \varepsilon_3)^2 \quad \left(\bar{\boldsymbol{\varepsilon}}^V\right)^2 = \left(\varepsilon^V\right)^2 = 2\varepsilon_5^2$$

$$\left(\bar{\varepsilon}^{III}\right)^2 = \left(\varepsilon^{III}\right)^2 = \frac{1}{2+\beta^2}(\beta\varepsilon_1 + \varepsilon_2 + \varepsilon_3)^2 \quad \left(\bar{\boldsymbol{\varepsilon}}^{VI}\right)^2 = \left(\varepsilon^{VI}\right)^2 = 2\varepsilon_6^2 \tag{31}$$

where ε_1 to ε_6 are strain components in material coordinate system.

A single strain energy mode is activated if only one of the modal strains is nonzero. Therefore, by solving the system of six equations obtained from Eq. (31) for each modal strain being non zero, the expressions for the modal strains given in terms of the strain components in material coordinate system can be obtained for each mode.

Orthotropic materials are defined by six modes, given in terms of six eigenvalues and six eigenvectors, therefore one can express six damage potentials that uniquely define these six modes in the form:

$$\Phi^I\left(y_d^I, y_h^I\right) = \frac{1}{2+\alpha^2}\left(1-d^I\right)\lambda_0^I(\alpha\varepsilon_1 + \varepsilon_2 + \varepsilon_3)^2 - \kappa^I h^I - \omega_0^I \leqslant 0$$

$$\Phi^{II}\left(y_d^{II}, y_h^{II}\right) = \frac{1}{2}\left(1-d^{II}\right)\lambda_0^{II}(\varepsilon_2 - \varepsilon_3)^2 - \kappa^{II} h^{II} - \omega_0^{II} \leqslant 0$$

$$\Phi^{III}\left(y_d^{III}, y_h^{III}\right) = \frac{1}{2+\alpha^2}\left(1-d^{III}\right)\lambda_0^{III}(\alpha\varepsilon_1 + \varepsilon_2 + \varepsilon_3)^2 - \kappa^{III} h^{III} - \omega_0^{III} \leqslant 0$$

$$\Phi^{IV}\left(y_d^{IV}, y_h^{IV}\right) = 2\left(1-d^{IV}\right)\lambda_0^{IV}\varepsilon_4^2 - \kappa^{IV} d^{IV} - \omega_0^{IV} = 0$$

$$\Phi^V\left(y_d^V, y_h^V\right) = 2\left(1-d^V\right)\lambda_0^V\varepsilon_5^2 - \kappa^V d^V - \omega_0^V = 0$$

$$\Phi^{VI}\left(y_d^{VI}, y_h^{VI}\right) = 2\left(1-d^{VI}\right)\lambda_0^{VI}\varepsilon_6^2 - \kappa^{VI} d^{VI} - \omega_0^{VI} = 0 \tag{32}$$

Note that for transversely isotropic materials, there are only five distinct eigenvalues, i.e. principle material stiffnesses so the number of modes can be reduced to four, with the fifth equivalent to sixth mode. For the material analysed here, the second and fourth principle stiffnesses have similar values, due to the fact that C_{23} is significantly smaller than C_{22}.

3. Mesoscale modelling of unidirectional and orthotropic composites

In order to justify the assumptions that this model is based on, made in the previous sections, a number of mesoscale models and loading conditions were considered. The validation of the assumption that damage induced changes in the material stiffness tensor at the continuum scale do not affect symmetries of the tensor, i.e. the direction of the tensor eigenvectors was one of the key steps. Further, the mesoscale

Table 1

Fibre material properties used in mesoscale model simulations (MAT_002).

E_x	$2.654 \bullet 10^5$ MPa	ν_{yx}	0.0126	G_{xy}	$1.550 \bullet 10^4$	MPa
E_y	$1.298 \bullet 10^4$ MPa	ν_{zx}	0.0126	G_{xz}	$1.550 \bullet 10^4$	MPa
E_z	$1.298 \bullet 10^4$ MPa	ν_{yz}	0.206	G_{yz}	$5.380 \bullet 10^3$	MPa

modelling was intended to improve understanding of the material behaviour and to aid in definition of material characterisation required for the damage model. A representative volume element (RVE) of the composite material with unidirectional fibre reinforcement was modelled using finite element (FE) method as shown in Fig. 1. The main composite constituents were modelled separately, i.e. fibres, matrix and their interface each having its own mechanical properties.

The mesoscale models of the RVE shown in Fig. 1 were generated in the commercial code Digimat [14]. RVE of a unidirectional composite comprised 16 fibres randomly distributed in matrix representative of a

transversely isotropic material. Note that the model has the properties of a repeating/periodic unit cell, as presented in Fig. 1-b) and thus satisfies the requirements for the RVE [15,16].

The RVE model, a cube with edge length of 26 μm, had the fibre volume fraction of 50% and the fibre diameter of 5 μm. The model consisted of 100,000 under integrated hexagonal solid elements (one integration point) of equal size, where isotropic and orthotropic elastic models (MAT_001 and MAT_002) [17], were used for matrix and fibre material, respectively. The matrix and fibre mechanical properties, used in the models, were determined experimentally. The value for the matrix Young's modulus was $E = 4668MPa$ and Poisson ratio $\nu = 0.4$. The fibre material properties are listed in Table 1.

Two types of boundary conditions were used in the models: periodic boundary conditions on the opposite faces to represent material continuity and boundary conditions combined with the loading.

Plain strain state was imposed in the material to determine columns of the material stiffness tensor. Each model was successively loaded by
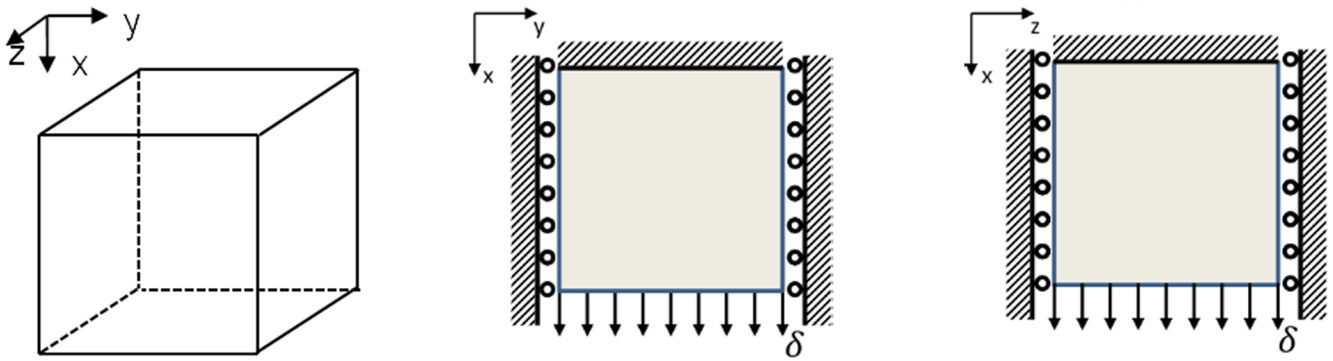

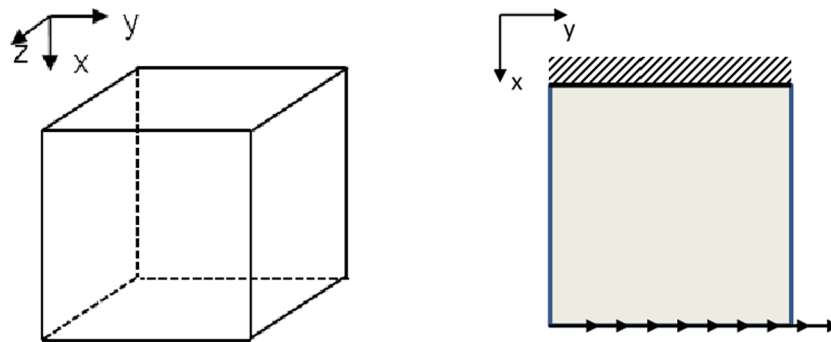**Fig. 2.** Loading and boundary conditions for normal load case.

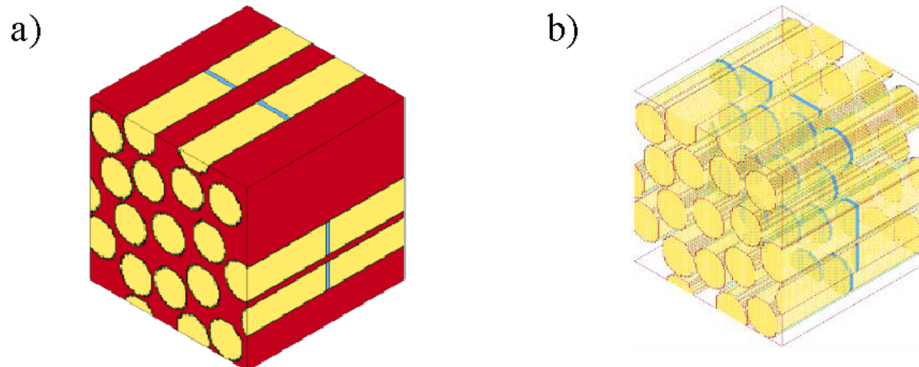**Fig. 3.** Loads and boundary conditions for shear load case.

Fig. 4. Mesoscale model with fibre cracking damage mechanism a) the whole model, b) highlighted fibre elements with reduced material properties representing the crack.
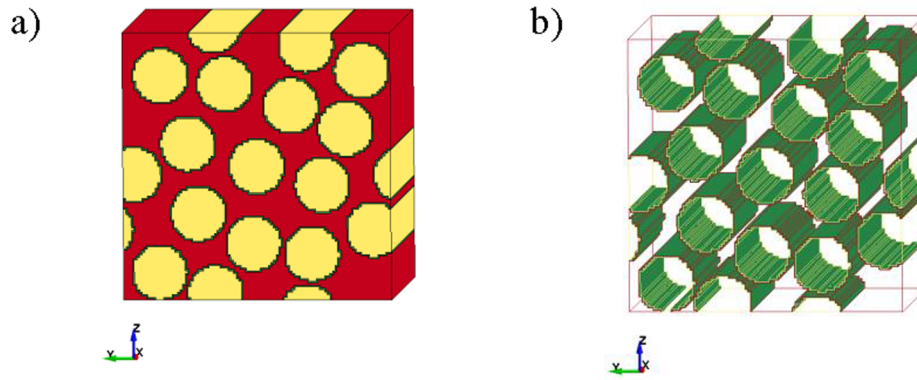
Fig. 5. Mesoscale model with fibre–matrix debonding damage mechanism a) the whole model, b) elements with with reduced material properties representing debond layer.
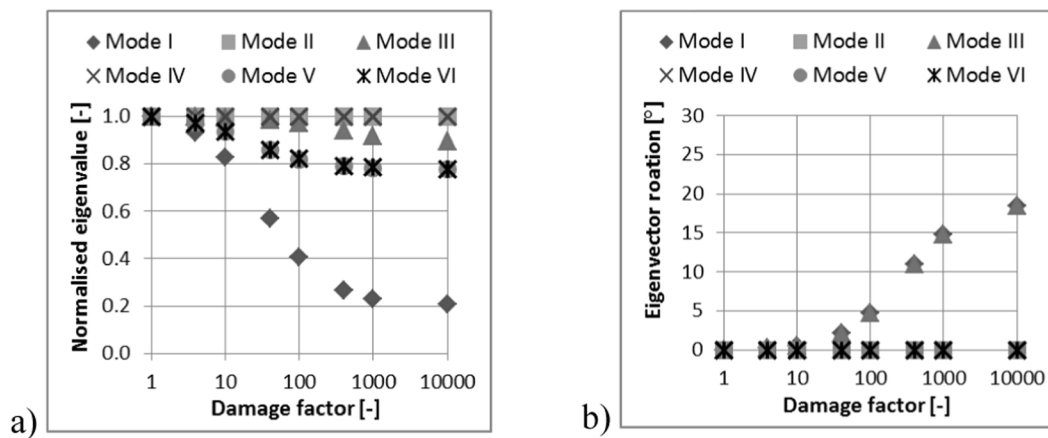

Fig. 6. Fibre damage effects: a) eigenvalue reduction, b) eigenvector roation.

six displacements – three normal displacements and three shear displacements. For normal loading cases one face of the RVE was loaded in tension, and the remaining faces were constrained from movement in the direction normal to them as schematically represented in Fig. 2 for the load in X direction. The load was applied by the set displacement of $\delta = 2.6 \cdot 10^{-5} mm$, which corresponds to the normal strain $\varepsilon_{ii} = 1 \cdot 10^{-3}$.

Plane shear strain was obtained by constraining one face in all directions and applying the load parallel to the RVE opposite face (Fig. 3). The load was applied as set displacement of magnitude $\delta = 2.6 \cdot 10^{-5} mm$ which corresponds to the true shear strain of $\varepsilon_{ij} = 5 \cdot 10^{-4}$ (or engineering shear strain $\gamma_{ij} = 1 \cdot 10^{-3}$). The applied strain magnitudes used in plain strain loading do not violate small strains assumption.

Fibre cracking was modelled by reduction of the material properties of one layer of the fibre elements as shown in blue in Fig. 4. Crack plane was normal to the fibre direction and situated in the middle of the RVE. It was modelled with the fibre elastic properties reduced by the different damage factors (4, 10, 40, 100, 400, 1000, 10000) to represent a range of damage extents.

Matrix damage was modelled by uniform reduction of stiffness properties applied to all matrix elements by a range of damage factors: 4, 10, 40, 100, 400, 1000 and 10,000. The Poisson's ratio remained unchanged. Fibre-matrix debonding was modelled by reduction of material properties of all matrix elements adjacent to the fibres as presented in green in Fig. 5. Debonded layer was modelled with isotropic material properties allowing for large deformations expected in the layer. The damage factors used in this model were 4, 10, 20, 40, 100, 400, 1000 and 10000.

Damage effects for specific damage mechanisms/cases were

incorporated in the models by reduction of the material stiffness for a set of specific elements within the RVE models, and the results averaged over the RVE. Following three damage cases were considered in this paper – fibre cracking, matrix microcracking and fibre–matrix debonding.

The calculation of material stiffness tensors was performed trough six simulations, each corresponding to either one of the three plain strain states or one of the three in plain shear states of the material. The stresses calculated in the finite element simulations resulting from these strain loading cases of the RVE allowed for determination of one material stiffness tensor column. The average stress values, used in equations (33), were determined using strain energy equivalence principle, i. e. the strain energy of the average stress was made equal to the strain energy of the calculated stress acting within the RVE for the applied strain.

As an example, calculation of the first column of the stiffness tensor using Eq. (2). For the loading defined as $\varepsilon_1 \neq 0$, $\varepsilon_2 = \varepsilon_3 = \varepsilon_4 = \varepsilon_5 = \varepsilon_6 = 0$ and the components of stress, determined from the finite element model of the RVE, the related members of the material stiffness tensor were determined as:

$$\sigma_1 = C_{11}\varepsilon_1 \Rightarrow C_{11} = \frac{\sigma_1}{\varepsilon_1} \quad \sigma_2 = C_{21}\varepsilon_1 \Rightarrow C_{21} = \frac{\sigma_2}{\varepsilon_1} \quad \sigma_3 = C_{31}\varepsilon_1 \Rightarrow C_{31} = \frac{\sigma_3}{\varepsilon_1}$$

(33)

The stiffness tensors were determined for undamaged material and material with different damage types. These damage types were analysed for a range of damage extents. For instance, fibre cracking was modelled by reducing the stiffness in one layer of all fibres located at the RVE midplane perpendicular to the fibre direction. Matrix
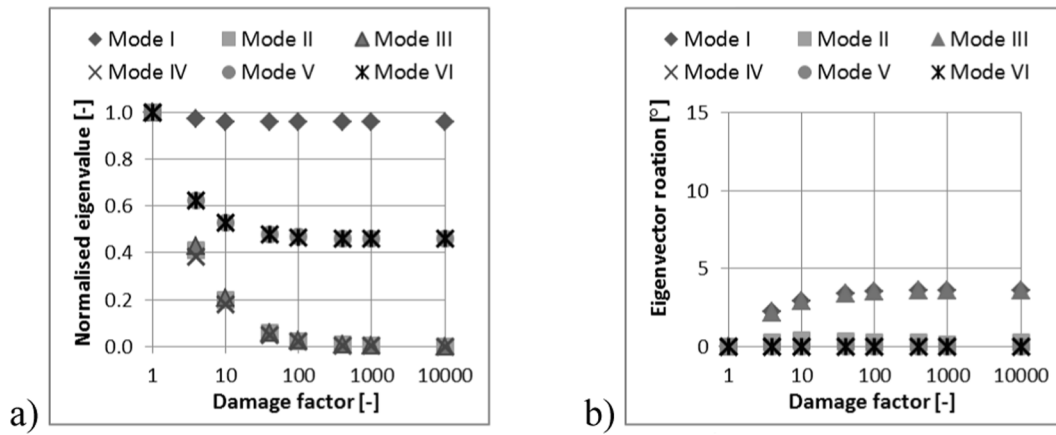
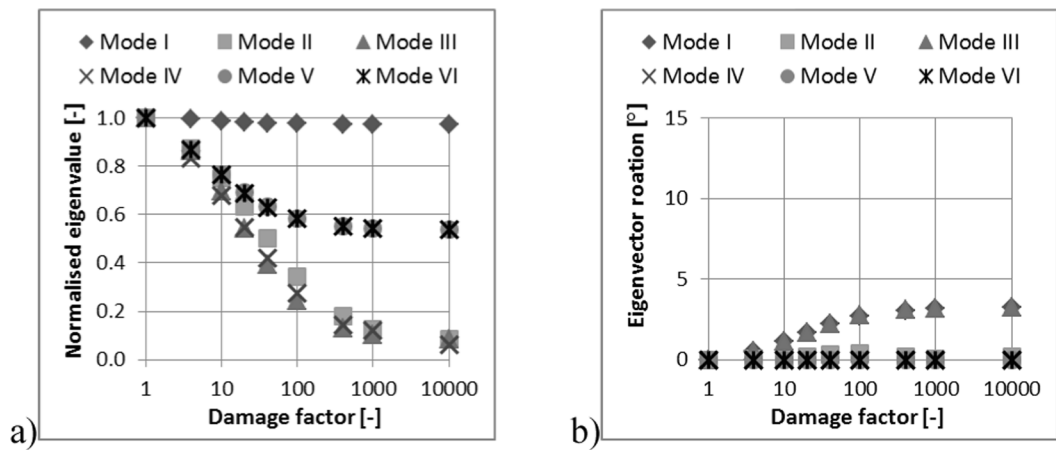**Fig. 7.** Matrix damage effects: a) eigenvalue reduction, b) eigenvector roation.

Fig. 8. Fibre-matrix debonding damage effects: a) eigenvalue reduction, b) eigenvector roation.

Table 2
Physical damage types and the affected damage parameters for unidirectional material.

Physical damage types	Affected damage modes (deformation modes)	Related general strain components - Eq. (35)
Fibre damage	$d^I, d^{III}, d^V, d^{VI}$	$\varepsilon_1, \varepsilon_2, \varepsilon_3, \varepsilon_5, \varepsilon_6$
Matrix cracking	$d^{II}, d^{III}, d^{IV}, d^V, d^{VI}$	$\varepsilon_2, \varepsilon_3, \varepsilon_4, \varepsilon_5, \varepsilon_6$
Matrix fibre debonding	$d^{II}, d^{III}, d^{IV}, d^V, d^{VI}$	$\varepsilon_2, \varepsilon_3, \varepsilon_4, \varepsilon_5, \varepsilon_6$

microcracking damage was modelled by reducing stiffness of the matrix (all matrix elements) in the RVE. The fibre–matrix debonding was modelled by reduction of the stiffness of the layer of the matrix elements adjacent to the all fibres. The stiffness of the elements affected by the introduced damage was reduced (divided by the scaling factor S for each damage mechanism incrementally in a number of steps ($S = 1, 10, 100, 1000, 10000, 100000$; see Fig. 6) to determine the influence of the progressive damage.

Stiffness tensors for all damage cases were determined and analysed in spectrally decomposed form, defined in terms of their eigenvalues and eigenvectors, defined in Section 2. Eigenvalues, obtained by the diagonalisation of the stiffness tensor, represent the material principal stiffnesses. For the investigated transversely isotropic material the undamaged material eigenvalues were:

$$\lambda^I = 139.5 \ GPa \quad \lambda^{II} = 5.8 \ GPa \quad \lambda^{III} = 16.1 \ GPa \tag{34}$$
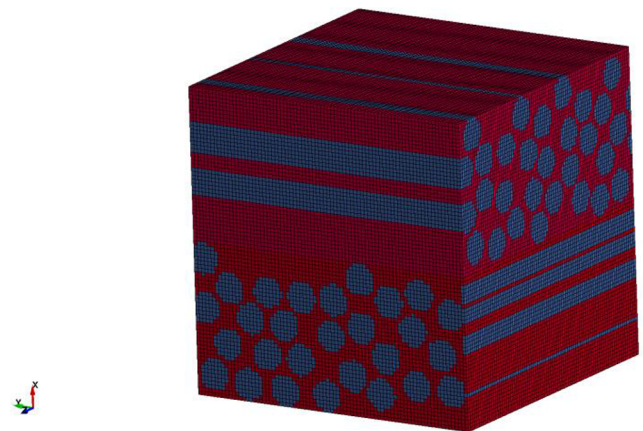

Fig. 9. RVE Finite Element model used for orthotorpic composite modelling: fibres material in blue and matrix material in red. (For interpretation of the references to colour in this figure legend, the reader is referred to the web version of this article.)

$$\lambda^{IV} = 5.7 \ GPa \cong \lambda^{II} \quad \lambda^V = 11.0 \ GPa \quad \lambda^{VI} = 11.0 \ GPa = \lambda^V$$

Note, for this material λ^{II} and λ^{IV} have a very similar value. Analysis of the eigenvalues without considering eigenvectors offers limited information in assessment of damage. The shear related eigenvectors of the stiffness tensor (v^{IV}, v^V and v^{VI}) are known and do not depend on the
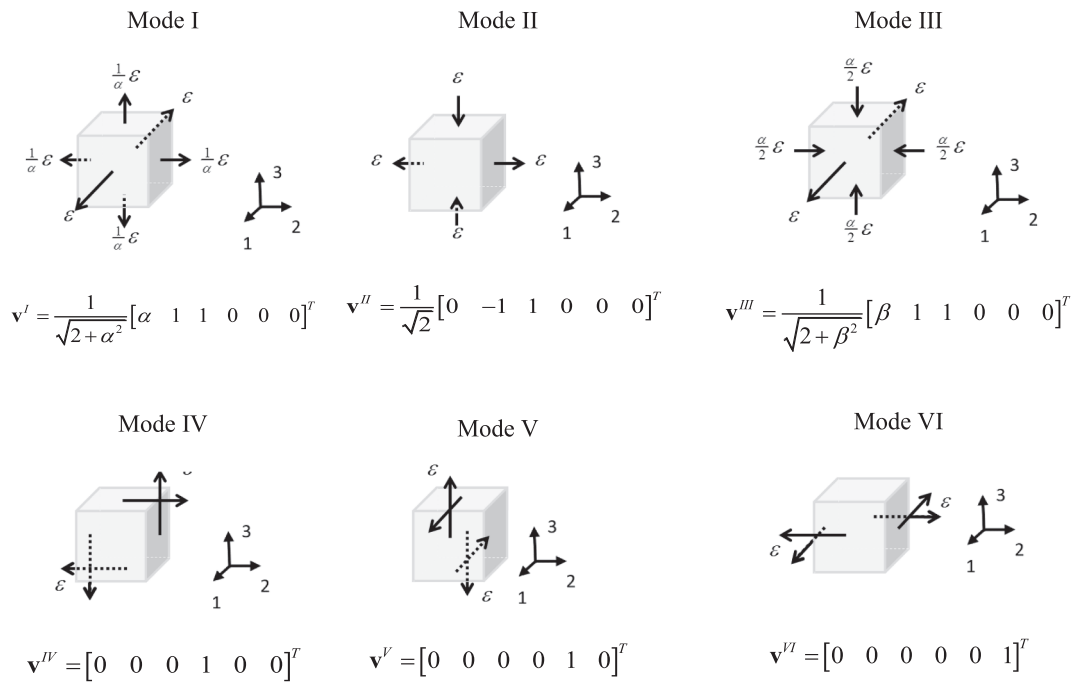
Mode I

Mode II

Mode III

$$\mathbf{v}^{I} = \frac{1}{\sqrt{2+\alpha^2}}\begin{bmatrix} \alpha & 1 & 1 & 0 & 0 & 0 \end{bmatrix}^{T} \qquad \mathbf{v}^{II} = \frac{1}{\sqrt{2}}\begin{bmatrix} 0 & -1 & 1 & 0 & 0 & 0 \end{bmatrix}^{T} \qquad \mathbf{v}^{III} = \frac{1}{\sqrt{2+\beta^2}}\begin{bmatrix} \beta & 1 & 1 & 0 & 0 & 0 \end{bmatrix}^{T}$$

Mode IV

Mode V

Mode VI

$$\mathbf{v}^{IV} = \begin{bmatrix} 0 & 0 & 0 & 1 & 0 & 0 \end{bmatrix}^{T} \qquad \mathbf{v}^{V} = \begin{bmatrix} 0 & 0 & 0 & 0 & 1 & 0 \end{bmatrix}^{T} \qquad \mathbf{v}^{VI} = \begin{bmatrix} 0 & 0 & 0 & 0 & 0 & 1 \end{bmatrix}^{T}$$

Fig. 10. Graphical representation of the single deformation modes.

Table 3
Characteristics of the eigenmodes for unidirectional mesoscale material.

Mode	Critical strain [%]	Principal stiffness λ^i [GPa]	Energy limit ω_0^i [kJ/m^3]	Dominant damage type
I	1.82	139.5	46684.8	fibre
II	0.94	5.8	524.0	matrix
III	3.12	16.1	15794.3	matrix
IV	0.95	5.7	518.7	matrix
V	0.39	11.0	164.5	matrix
VI	0.40	11.0	171.3	matrix

Table 4
Unidirectional material properties used for single element verification.

Density [g/cm^3]	ρ	1.622
Stiffness [GPa]	E_1	165.00
	$E_2 = E_3$	9.84
	$G_{12} = G_{31}$	4.98
	G_{23}	3.00
Poisson's ratio [-]	$\nu_{21} = \nu_{31}$	0.0169
	ν_{32}	0.4535
Damage threshold [MPa]	ω^I	46.210
	$\omega^{II} = \omega^V$	2.096
	ω^{III}	7.836
	$\omega^{IV} = \omega^{VI}$	3.138
Critical damage variable	d^I	0.3
	$d^{II} = d^{III}$	0.5
	$d^{IV} = d^V = d^{VI}$	0.7

eigenvalues (λ^I to λ^{VI}) for transversely isotropic materials. The eigenvectors that may be subjected to change due to damage are eigenvectors $\mathbf{v}^I$, $\mathbf{v}^{II}$ and $\mathbf{v}^{III}$. Change in orientation of the eigenvectors was measured by the rotation angle defined as $\varphi^I = \arccos\left(\mathbf{v}_0^I \cdot \mathbf{v}_d^I\right)$, where the subscripts '0' and 'd' refer to undamaged and damaged material eigenvector, respectively. The eigenvectors of undamaged material were:

$$\mathbf{v}_0^I = \begin{bmatrix} 0.998 & 0.044 & 0.044 & 0 & 0 & 0 \end{bmatrix}^T \quad \mathbf{v}_0^{II}$$
$$= \begin{bmatrix} 0 & -0.707 & 0.707 & 0 & 0 & 0 \end{bmatrix}^T \tag{35}$$

$$\mathbf{v}_0^{III} = \begin{bmatrix} -0.062 & 0.706 & 0.706 & 0 & 0 & 0 \end{bmatrix}^T \quad \mathbf{v}^{IV} = \begin{bmatrix} 0 & 0 & 0 & 1 & 0 & 0 \end{bmatrix}^T$$

$$\mathbf{v}^{V} = \begin{bmatrix} 0 & 0 & 0 & 0 & 1 & 0 \end{bmatrix}^T \quad \mathbf{v}^{VI} = \begin{bmatrix} 0 & 0 & 0 & 0 & 0 & 1 \end{bmatrix}^T$$

The first eigenvector $\mathbf{v}^I$ was almost aligned with the fibre direction. Therefore, the first eigenvalue is associated with the longitudinal direction. This is consistent with the reduction of the first eigenvalue due to fibre damage, which was significant in comparison to other eigenvalue reductions, as can be observed in Fig. 6-a). As a consequence of this effect, the first and the third eigenvectors rotated significantly more compared to the other eigenvectors, see Fig. 6-b). The rotation of the eigenvectors reflects the material losing its anisotropy, i.e. dominant longitudinal stiffness. It is important to note that the rotation of eigenvectors $\mathbf{v}^I$ and $\mathbf{v}^{III}$ becomes significant when the effective fibres stiffness becomes comparable to the matrix stiffness due to the damage (damage factor over 100 in Fig. 6-b)). For damage factor of 100, the rotation of eigenvectors I and III is below 5°. Consequently, the assumption that eigenvectors remain invariant is justified.

The similar analysis was carried out for the matrix damage related effects. For uniform matrix damage the highest (and equal) reduction was observed for the second, third and fourth eigenvalues (Fig. 7). The uniform damage in the matrix does not have significant impact on the eigenvector basis rotation – none of the eigenvectors rotated more than 5° even when matrix stiffness was reduced by five orders of magnitude (see Fig. 8).

The fibre–matrix debonding damage modelling results were similar to the uniform matrix damage results. The reduction of the second, third and fourth eigenvalue is almost equal as it is for the mode five and six, Fig. 7-a). The eigenvector rotation due to the fibre–matrix debonding damage was insignificant, as illustrated in Fig. 7-b).

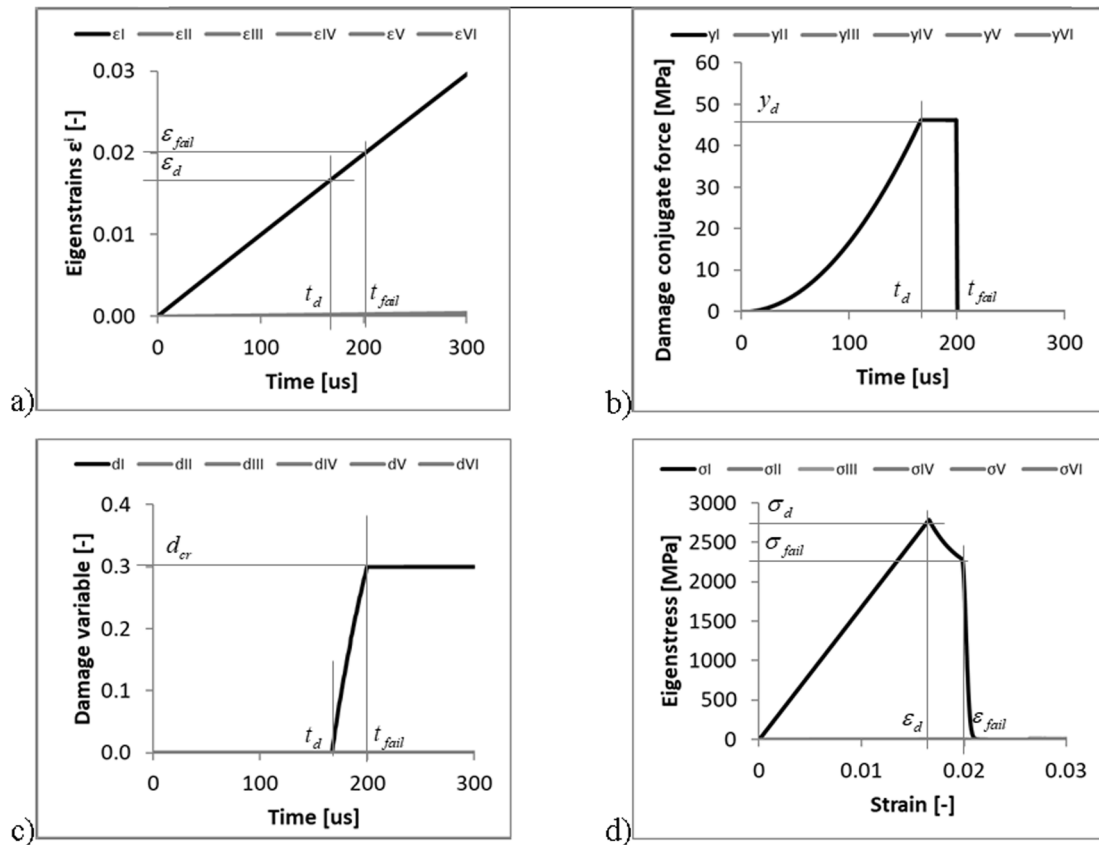The most important conclusions from mesoscale damage modelling are:

Fig. 11. State variables histories from the single element tests for Mode I loading: a) strain; b) Damage conjugate force; c) damage variable; d) stress strain curve.
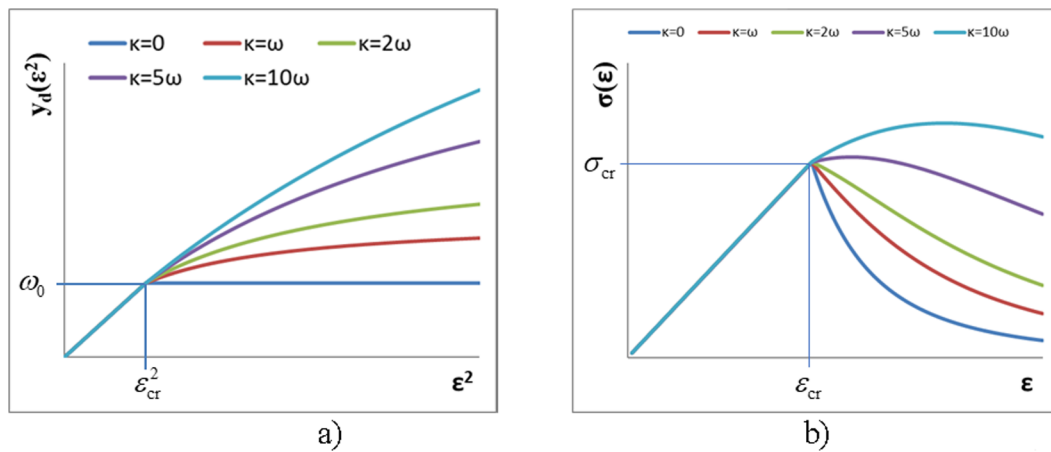

Fig. 12. Analytical solution for damage conjugate force (a) and stress strain curve (b) obtained for a range of evolution energies.

- the eigensystem of the material remains unchanged due to the matrix damage;
- the small (negligible) rotation of eigensystem is characteristic for fibre damage up to the critical fibre damage (damage level for which the fibre effective stiffness approaches the matrix stiffness);
- modelling of damage can be based on the reduction of the principal stiffnesses without change of direction of the eigenvectors. This is conditional to the extent of the fibre damage, as described above.

The data presented in Figs. 2 to 4 is summarised in the Table 2. which relates physical damage types, affected damage parameters and the general components of strain.

The procedure outlined for the unidirectional (transversely

isotropic) composites was repeated for orthotropic composite material, using the RVE finite element model shown in Fig. 9. The RVE can be interpreted as a being representative of two plies of a cross-ply laminate, which was used here as a mesoscale model of an orthotropic material. The stiffness tensor and corresponding set of six eigenvalues and the eigenvectors obtained for this architecture and material properties of experimentally tested orthotropic material is given below:
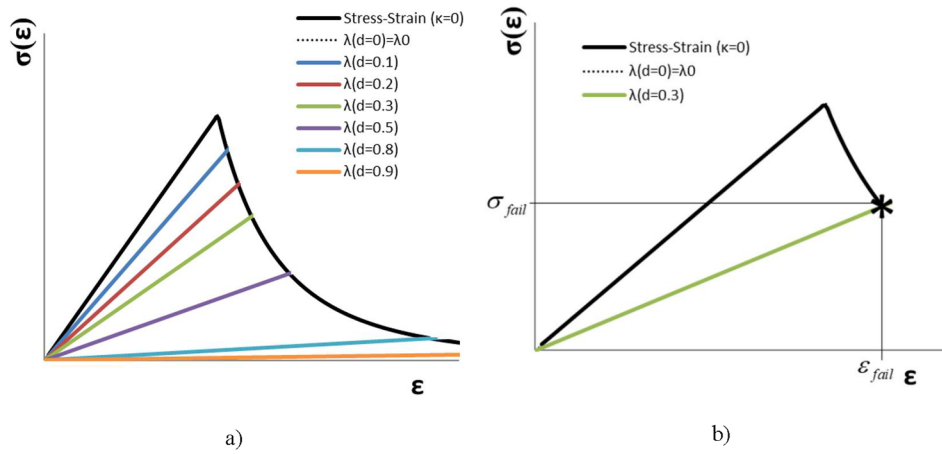
Fig. 13. a) Modal Stress modal strain curve and a family of unloading curves for a range of damage variables for deformation mode I b) modal stress – modal strain curve with unloading at d = 0.3.

Table 5
Material parameters determined for the orthotropic composite materials.

GPa / [-]		MJ/m³		[-]		MJ/m³	
E_x	10.0	ω_0^I	36.5	d_{cr}^I	0.3	κ^I	73.0
$E_y = E_z$	68.5	ω_0^{II}	16.0	d_{cr}^{II}	0.3	κ^{II}	32.0
G_{yz}	4.57	ω_0^{III}	6.3	d_{cr}^{III}	0.5	κ^{III}	12.6
$G_{zx} = G_{xy}$	3.57	ω_0^{IV}	3.1	d_{cr}^{IV}	0.7	κ^{IV}	6.2
ν_{yz}	0.039	ω_0^V	2.1	d_{cr}^V	0.7	κ^V	4.2
$\nu_{zx} = \nu_{xy}$	0.045	ω_0^{VI}	3.1	d_{cr}^{VI}	0.7	κ^{VI}	6.2

Fig. 14. Shock velocity vs particle velocity for the composite material considered: data points with error bars obtained in the plate impact tests and linear approximation of the data.

$$C = \begin{bmatrix} 10.00 & 0.47 & 0.47 & 0 & 0 & 0 \\ 0.47 & 68.63 & 2.70 & 0 & 0 & 0 \\ 0.47 & 2.70 & 68.63 & 0 & 0 & 0 \\ 0 & 0 & 0 & 7.14 & 0 & 0 \\ 0 & 0 & 0 & 0 & 9.14 & 0 \\ 0 & 0 & 0 & 0 & 0 & 7.14 \end{bmatrix} GPa \qquad (36)$$

$$\lambda^I = 71.3 \; GPa, \quad \mathbf{v}^I = [0.011 \quad 0.707 \quad 0.707 \quad 0 \quad 0 \quad 0]^T,$$

$$\lambda^{II} = 65.9 \; GPa, \quad \mathbf{v}^{II} = [0 \quad -0.707 \quad 0.707 \quad 0 \quad 0 \quad 0]^T,$$

$$\lambda^{III} = 10.0 \; GPa, \quad \mathbf{v}^{III} = [-0.9999 \quad 0.008 \quad 0.008 \quad 0 \quad 0 \quad 0]^T,$$

$$\lambda^{IV} = 7.1 \; GPa, \quad \mathbf{v}^{IV} = [0 \quad 0 \quad 0 \quad 1 \quad 0 \quad 0]^T,$$

$$\lambda^V = 9.1 \; GPa, \quad \mathbf{v}^V = [0 \quad 0 \quad 0 \quad 0 \quad 1 \quad 0]^T,$$

$$\lambda^{VI} = 7.1 \; GPa = \lambda^{IV}, \quad \mathbf{v}^{VI} = [0 \quad 0 \quad 0 \quad 0 \quad 0 \quad 1]^T.$$

where the coefficients α and β are equal to 0.015 and, −131 respectively. The high value of β makes the third eigen vector parallel to the through thickness direction (X), with negligible influence of the material properties in Y and Z directions. The material properties given in Eq. (36) were used for calculation of the orthotropic material properties given in Table and modelling of plate impact tests and hard projectile impact tests in described in Section 4. The RVE dimensions were chosen so that through thickness size of the RVE model was equivalent to the ply thickness of the experimentally tested orthotropic material.

3.1. Calculation of the material properties for damage model – Critical energy limits

Young's moduli, shear moduli and Poisson's ratios define linear elastic material behaviour and the material stiffness tensor, including its eigenvalues and eigenvectors. Additional parameters needed to define the damage initiation and evolution are critical damage initiation energy (threshold energy). The critical damage initiation energy ω_0^i can be determined by the mechanical tests which activate single strain energy modes. Experimental activation of a single strain energy mode can be achieved when the sample loading results in a strain state determined by a single modal strain defined in Eq. (31). Six single strain energy modes and the related eigenvectors of the material stiffness tensor for orthotropic materials are illustrated in Fig. 10. Note, material characterisation for modes I and III require constrained uniaxial tests whereas mode II requires uniform biaxial loading test. Second, fourth, fifth and sixth modes are the shear modes which can be achieved in the shear tests, for
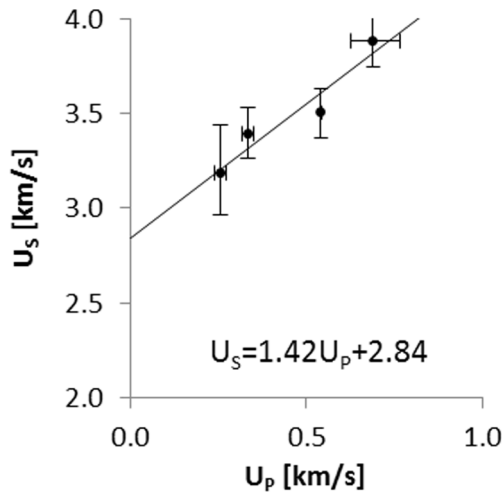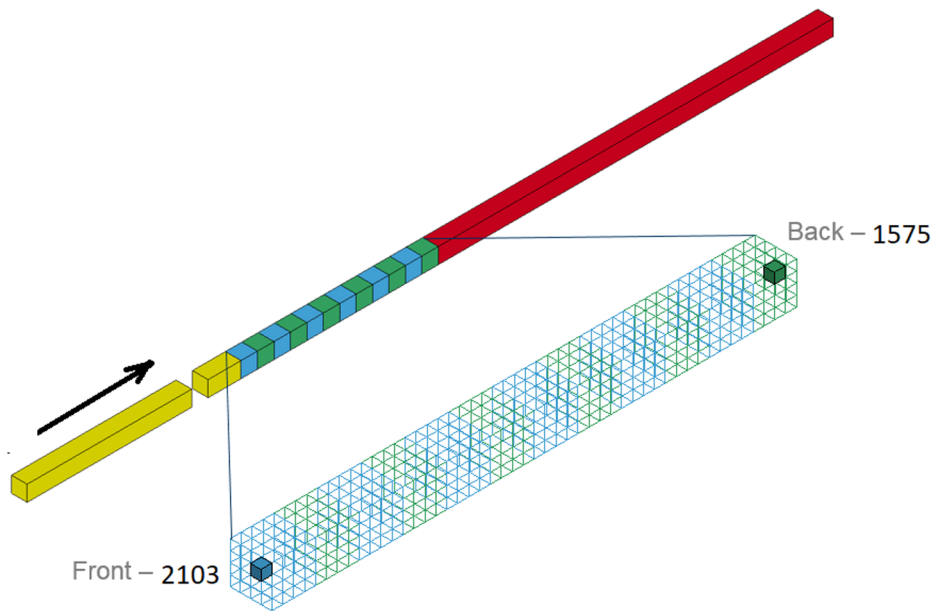
Fig. 15. FE model for plate impact test in through thickness direction with enlarged target mesh and elements used to generate stress time histories; the flyer and cover plates are shown in (yellow), composite taget plate has plies shown in green and blue and PMMA back plate is shown in red. (For interpretation of the references to colour in this figure legend, the reader is referred to the web version of this article.)
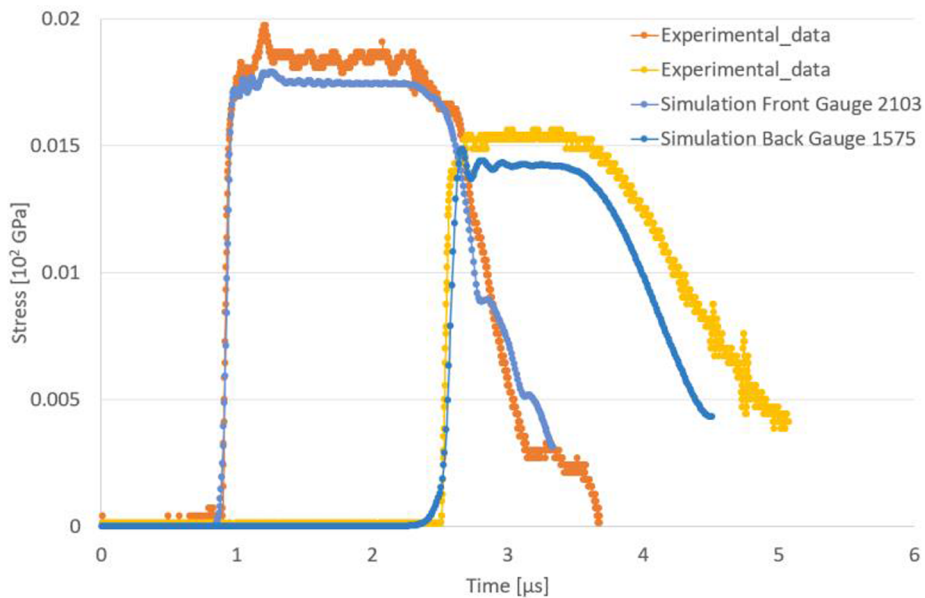

Fig. 16. Stress histories obtained in plate impact test for a 3.8 mm thick composite plate in the through thickness direction at impact velocity of 504 m/s [18].

instance IOSIPESCU shear test. For the unidirectional composites, the second and the fourth modes are equivalent and consequently characterised by the same energy limit. The same holds for modes V and VI.

In this work, the critical damage initiation energy thresholds were established by the mesoscale model simulations designed to activate a single strain energy mode in the series of separate simulations. For Mode I, the strain energy threshold was established at the point where maximum stress levels in fibres reached fibre strength level. For the other modes, the critical energy levels were established by comparison maximum von Mises stress in matrix with the matrix material strength. Note, this is possible because of the linear elastic material response up to damage initiation point. Calculated critical damage initiation energy thresholds and the corresponding damage mechanism for unidirectional material are presented in the Table 3.

The results show that the fibre related first mode has the highest energy limit. For the other five modes, the matrix was found to be more critical constituent.

4. Model validation and impact modelling

The constitutive model described in Section 2 was implemented into explicit nonlinear finite element code DYNA3D [23] and coupled with the vector Shock Equation of State, developed in [21]. Verification and validation of the constitutive model were conducted in the series of single element tests, simulation of plate impact tests and sphere projectile impacts.
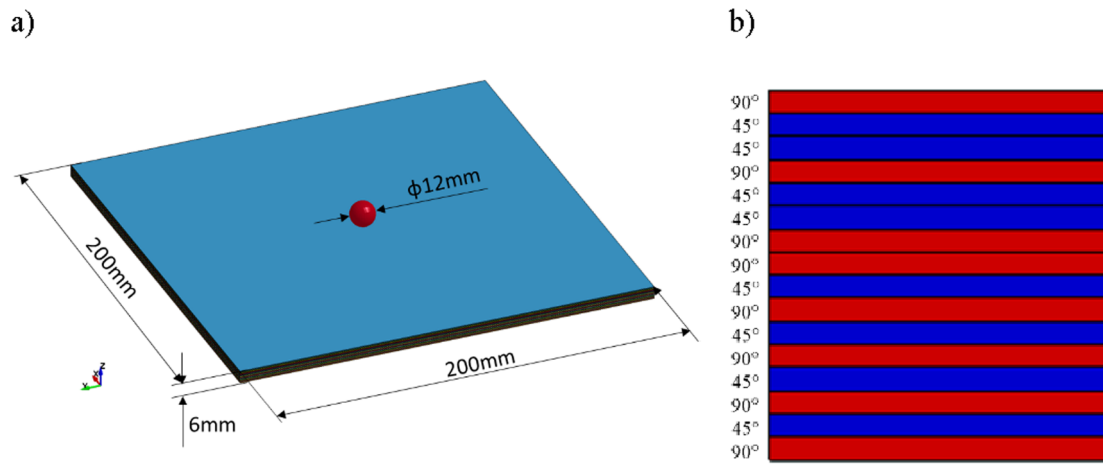
a)

b)

Fig. 17. Hard projectile impact test: a) finite element model (hexagonal mesh not displayed for the resolution reasons), b) composite material layup;

4.1. Single element tests

The new material model was first verified in a series of single element tests for which analytical solutions were known. The first set of tests verified a version of the model which allows for constant damage hardening and failure. In the second set of single element tests the variable damage hardening part of the model was activated allowing for more realistic modelling of progressive damage and failure.

Verification of the model implementation was performed for the loading conditions presented in Figure, for which the analytical solutions were known. The material model input data used for simulation of the unidirectional composite is given in Table 4. Note, the critical energy for damage initiation and critical damage parameter for complete failure were the input parameters for the constitutive model. Damage initiation for the first mode was determined from the fibres failure strain. This was justified by the fact that, in the mesoscale modelling, the first eigenstrain was almost exactly equal to the fibre strain. Critical strains for the shear modes were calculated using the matrix shear strength. The second and the fourth mode parameters are the same, as these modes share the similar eigenvalue. The damage initiation energy threshold for the third mode was determined from the mesoscale simulations. The state variable histories for the Mode I and the corresponding stress strain curve are given in Figure. These results confirm that a single mode is activated as the all non zero variables in this test correspond to Mode I. For the constant modal strain rate loading, liner elastic response was obtained up to damage initiation, when the damage conjugate force reaches the critical value of $46MPa$ at the response time $t_d = 160\mu s$. For the loading increasing monotonically with time, the Mode I damage variable increases to the critical value of $d_{cr} = 0.3$ at the response time $t_d = 200\mu s$. When the critical damage value is reached, the material loses its load carrying capacity and the stress is set to zero over the subsequent 100 calculation timesteps. Similar results are obtained for the other modal loadings. The simulation results are equivalent to the corresponding analytic solutions, which confirms that the model was implemented correctly.

The single element tests results shown in Fig. 11 were obtained with a minimum set of material damage parameters, which consists of damage initiation energy thresholds and the critical damage variables for total material failure for the six deformation modes.

The second stage in the single element verification considered the variable damage evolution rate part of the material model. As already stated, the model uses a linear damage evolution law (linear function of the conjugate force Eq. (20)) which allows for more realistic modelling of progressive damage/material softening.

$$\Phi = y_d + (y_h - \omega_0) = 0, \quad y_d = (1-d)\lambda_0\varepsilon^2, \quad y_h = \kappa h, \qquad (37)$$

In Eq. (37) the evolution of the damage potential is controlled via the damage evolution variable h which can have value between 0 and 1.

The material parameters for the damage model can be determined from a series of six modal experiments where a single deformation mode is generated in specimens and the modal stress – modal strain curves recorded. Equally, one can analytically determine estimates for these parameters and their allowable ranges, as illustrated in Figure, where the evolution energy κ is defined in terms of the threshold energy ω_0.

In Fig. 12 the constant damage threshold behaviour corresponds to $\kappa = 0$ where stress decreases below σ_{cr} value at the fastest rate. One can observe that as κ increases the material softening decreases. For $\kappa = 5\omega_0$, which should be taken as a threshold value for this parameter, following damage initiation the material exhibits almost zero hardening rate. Further increase in the evolution variable resulted in a nonphysical damage hardening (for this material), as illustrated with the curve $\kappa = 10\omega_0$ in Fig. 12-b).

Determination of a critical damage parameter for deformation mode I is illustrated in Fig. 13, where (a) illustrates a stress strain curve obtained for one deformation mode and a family of possible unloading curves, which correspond to the damage variables ranging from zero to one. For a failure obtained at the stress – strain state denoted with asterisk in Fig. 13-b), one can calculate the stress at failure and the critical damage as:

$$d_{cr} = 1 - \sqrt{\frac{\sigma_{fail}}{\lambda_0\varepsilon_{fail}}} \qquad (38)$$

For the carbon fibre composites considered in this work, critical damage parameter for fibre failure dominated modes was determined to be $d_{cr} = 0.3$ and for the other deformation modes critical damage was taken to be $d_{cr} = 0.5$.

Material characterisation for the orthotropic composite material used in the simulations of the impact tests followed the approach described above, making use of the elastic and strength properties at the mesoscale level obtained from material manufacturer. Calculated constitutive model parameters are given in Table 5 and used in the following section for the numerical validation against the experimental data.

4.2. Plate impact tests

Plate impact tests are typical material characterisation experiments designed to determine material Hugoniot and Equation of State data [18–20]. At the impact of ideally parallel flyer plate and target plate, the materials in contact undergo uniaxial strain state and for the sufficiently high impact velocity, shock wave is generated and propagate through the both plates. In our plate impact experiments, the flyer plate and
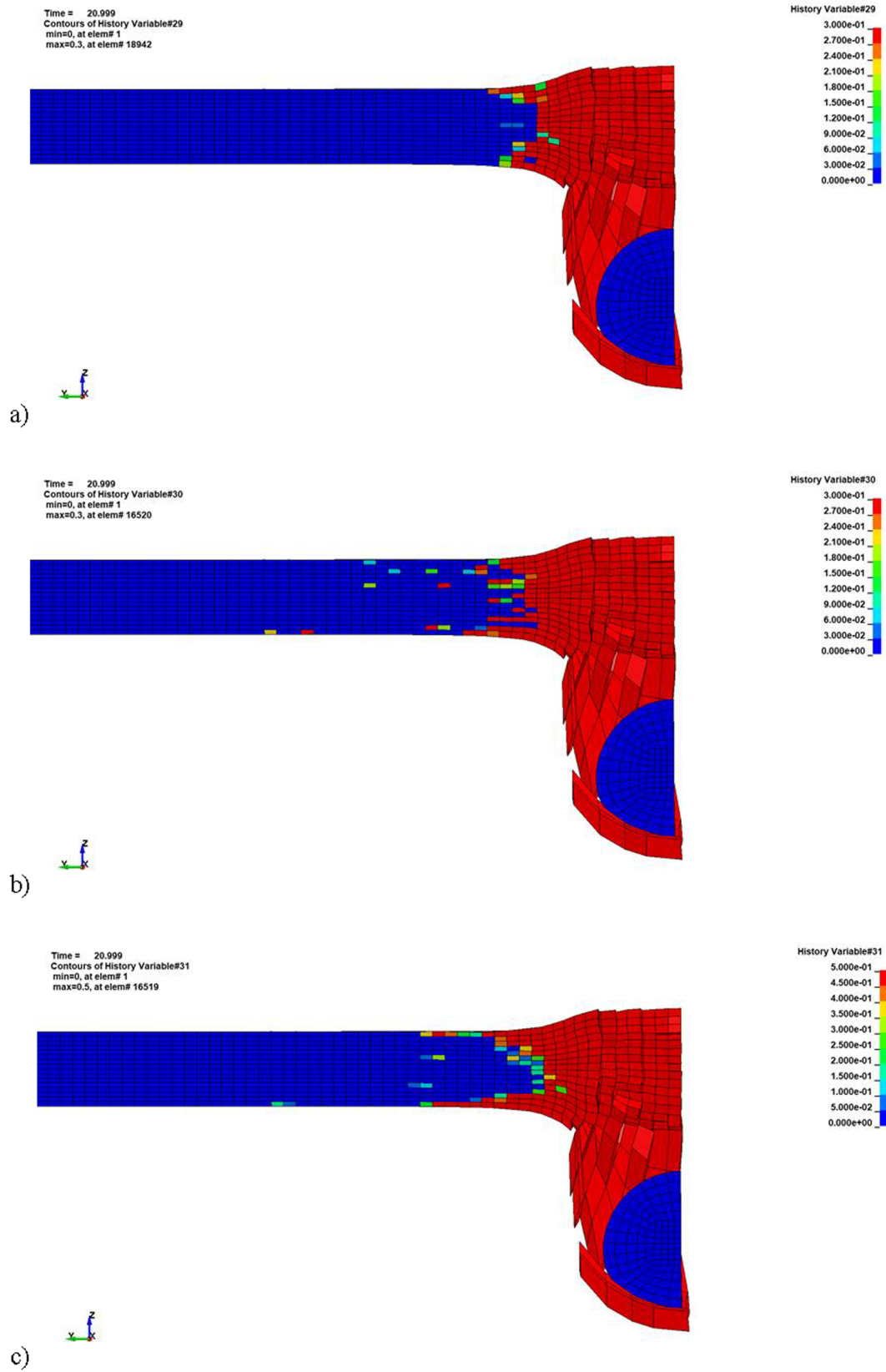
Fig. 18. Damage variables distribution thought the thickness of the composite target panel: a) damage mode I; b) damage mode II; c) damage mode III; d) damage mode IV; e) damage mode V; f) damage mode VI;
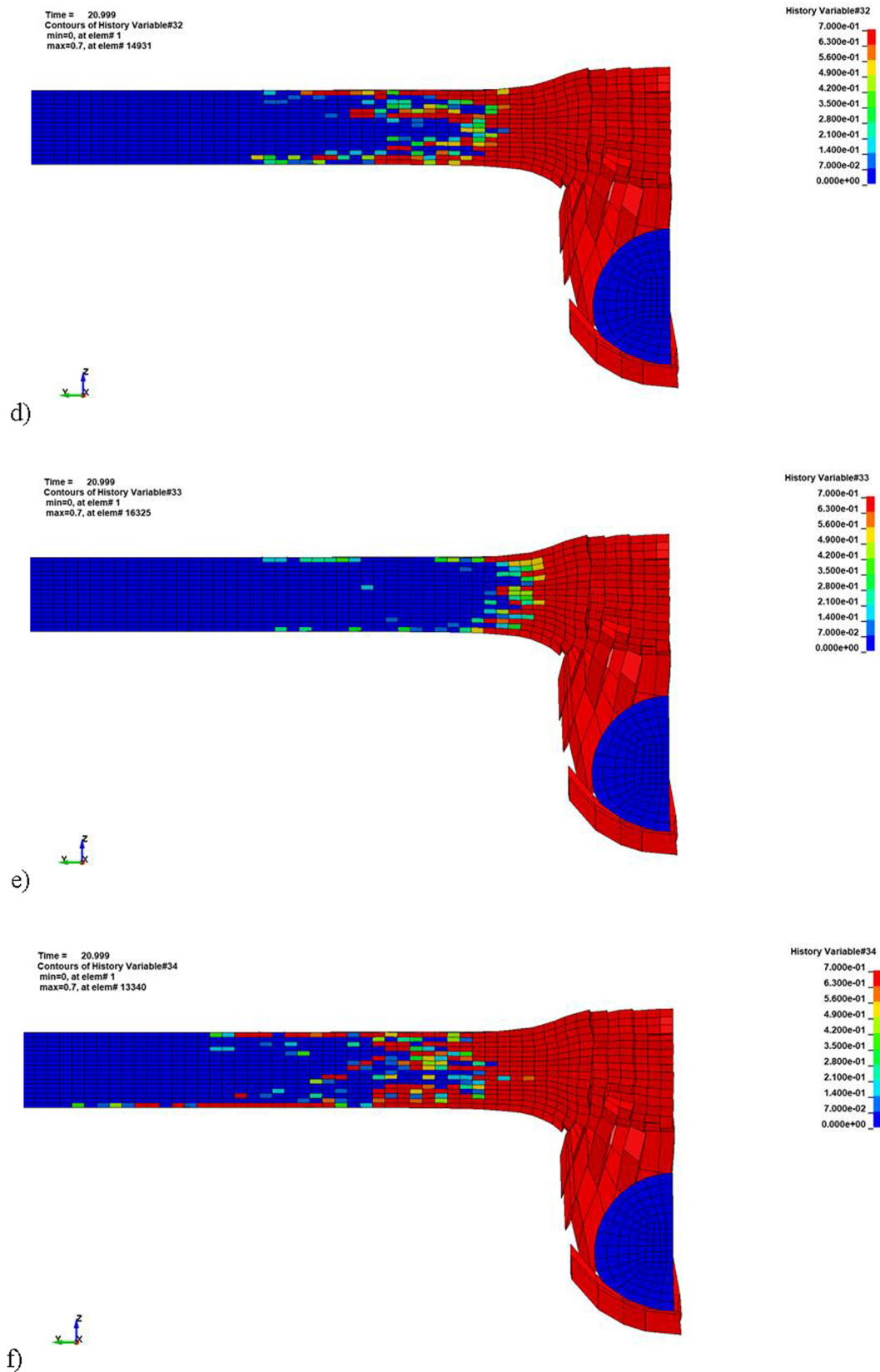
d)

e)

f)

Fig. 18. (*continued*).

target cover plate were made from aluminium. The rear side of the composite target was covered by PMMA backing plate.

A schematic representation of finite element model of plate impact test of the orthotropic carbon fibre composite in through thickness di-

rection is given in Figure. The model consists of under-integrated hexagonal solid elements with one integration point: 5 mm thick flyer plate was modelled with 30 elements in the impact direction; the 1 mm thick cover plate was modelled with 10 elements in the impact direction,

Table 6
Diameter of the modal damage zones thought the target thickness.

Mode	Maximum diameter [mm]	Minimum diameter [mm]	Ply number
I	28.0	22.0	
II	30.0	27.0	7/8
III	42.0	28.0	7
IV	60.0	34.0	8
V	38.0	28.0	8
VI	74.0	52.0	7

3.8 mm thick composite plate modelled with 32 elements along the impact direction (4 elements per ply) and 12 mm thick PMMA modelled with 100 elements in the impact direction. Aluminium and PMMA are modelled as an isotropic-elastic–plastic-hydrodynamic model, the material data for which was taken from the literature (Steinberg 1991). The carbon fibre epoxy target plate was modelled as a quasi-orthotropic material with the elastic and strength properties obtained from material manufacturer. The material parameters required for the shock equation of state for this material were determined through plate impact tests. The experimental data from the plate impact tests, in the form of Shock velocities U_S vs. particle velocity U_P, is shown in Fig. 14. In the linear approximation of the shock velocity as a function of particle velocity $U_S = C + S_1 U_P$, the coefficients have the following values $C = 2.84\ km/s$ and $S_1 = 1.42$.

The simulation results were assessed in terms of stress histories obtained at the front and at the back of the composite target plate, using the elements 2013 and 1575, respectively (shown in Fig. 15). The stress history recordings from the front and the back stress gauges, published in [18], were compared to the simulation results obtained with the newly developed constitutive model in Fig. 16. A good agreement between numerical and experimental results can be observed in terms of stress levels, loading pulse duration and shape and shock wave speed. Note, the slope of the unloading part of the simulation curve obtained at the back of the target plate (back gauge) is very similar to the slope of the corresponding experimental curve. This indicates that the new constitutive model is accurately modelling progressive damage in the composite due to the shock loading. The average stress level behind the shock is underestimated by 5% from the experimentally observed. The rising parts of the stress history curves calculated and experimental coincide indicating that the shock computed wave speed was close to the experimental shock wave speed.

4.3. Hard projectile impact test on a flat composite panel

Numerical validation of the newly developed constitutive model was completed by modelling the hard projectile impact on the flat composite target [20]. The composite plate is 6 mm tick and consists of 16 orthotropic plies with the ply thickness of 0.375 mm. The initial/impact speed of the steel projectile was 1200 m/s.

Due to the local nature of the deformation process in this test, in-plane dimensions of the finite element model are reduced from 300 mm to 200 mm as shown in Fig. 17. The composite target was modelled with one hexagonal solid element per the ply thickness, corresponding to a total of 640,000 hexagonal elements used for the target. The sphere was modelled with 2,432 solid elements, using the butterfly mesh.

The experimental results were given in terms of hole size generated at impact and the extent of delamination developed through the thickness of the composite panel. These results are compared to the numerical results obtained at response time t = 20.8 μs after the initial projectile-target contact, which is over 4 μs after the projectile completely penetrated the target. Simulation results agree well with the experiments in terms of overall kinematics of deformation and damage distribution. The projectile penetrated through the thickness of the panel, creating a hole in the material. The experimentally determined hole diameters, obtained in two perpendicular directions are 11.7 mm and 12.8 mm, whilst the corresponding numerical results are 12.0 mm and 12,14 mm, respectively. The relative errors for these two results are, respectively, 2.5% and 5.2%.

Quantitative analysis of damage through the thickness of the panel was carried out by using the six modal damage variables plotted in Fig. 18. For the sake of clarity, the figure shows one half of the cross section through the middle of the model, where the red elements represent total failure and the blue elements represent virgin material. Damage distribution through the thickness of material for all six modes is of hourglass shape which agrees very well with the experimental observation. Maximum and minimum damage dimeters measured from the numerical results for each damage mode are given in Table 6.

One can observe that fibre failure driven damage modes (first and second) developed locally in vicinity of the generated hole and did not propagate far away from the impact zone. Damage distribution obtained at the back of the target panel was similar in shape and size to the damage obtained at the front ply.

Damage eigen modes affiliated with three delamination modes are Mode III, Mode IV and Mode VI for opening, shear and tearing modes, respectively. However, the available experimental data were the C-scans of delamination opening mode, as the shear modes do not necessarily cause the free surface opening. Consequently, a comparison of the numerical results for Mode III with the delamination size distribution through thickness is shown in Fig. 19, where the maximum delamination calculated in the simulation is within 5% of the experimental results.

5. Conclusion

A series of numerical simulations was conducted using the newly developed constitutive model described in this work. The model was implemented in LLNL Dyna3d 2004 [23] and coupled with the vector Equation of State [21]. The verification was conducted in a series of single element modal simulations, with the results correctly reproducing the analytical solutions.

Numerical validation was conducted against the available experimental data from plate impact tests and hard projectile impact tests. The constitutive model accurately predicted the composite material response
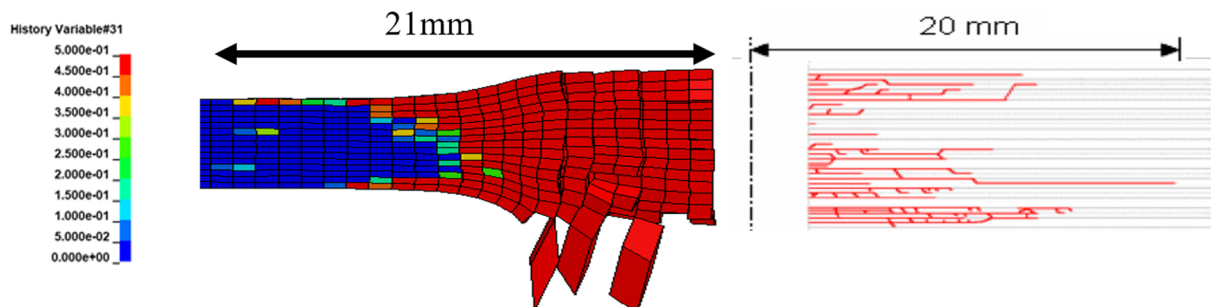

Fig. 19. Damage mode III variable distribution (left) that corresponds to delamination obtained from the post impact C scans experimental results (right).

to the considered shock loading in through thickness direction, including the shock wave speed and progressive damage in the composite due to the shock loading. The constitutive model accurately predicted the kinematics of deformation, including the damage distribution through the target thickness and size of the delamination zone generated at high velocity impact. The size of the delaminated zone obtained in these simulations was within 5% of the size calculated from the post impact analysis of the tested panels [5].

CRediT authorship contribution statement

Rade Vignjevic: Conceptualization, Methodology, Formal analysis, Investigation, Resources, Writing – original draft, Supervision, Project administration, Funding acquisition. **Nenad Djordjevic:** Methodology, Software, Validation, Formal analysis, Investigation, Writing – review &

editing, Visualization, Supervision, Project administration. **Agata Galka:** Methodology, Software, Validation, Formal analysis, Investigation, Writing – original draft, Visualization. **Gareth Appleby-Thomas:** Validation, Formal analysis. **Kevin Hughes:** Writing – review & editing.

Declaration of Competing Interest

The authors declare that they have no known competing financial interests or personal relationships that could have appeared to influence the work reported in this paper.

Appendix

A-1. Integration of damage variable rate

Eq. (26) for rate of change of damage variable, obtained from the consistency condition, is written with damage variable and its time derivative on the left side and strain and its time derivative on the right side:

$$\frac{1}{(1-d^i)}\frac{dd^i}{dt} = \frac{2\lambda_0^i \boldsymbol{\varepsilon}^i}{\kappa^i + \lambda_0^i (\overline{\boldsymbol{\varepsilon}}^i)^2}\frac{d\boldsymbol{\varepsilon}^i}{dt} \tag{A.1}$$

This equation can be integrated and solved in the following steps as:

$$\int \frac{1}{(1-d^i)}dd^i = \int \frac{2\lambda_0^i \boldsymbol{\varepsilon}^i}{\kappa^i + \lambda_0^i (\overline{\boldsymbol{\varepsilon}}^i)^2}d\boldsymbol{\varepsilon}^i \tag{A.2}$$

$$e^{-\ln(1-d^i)} = e^{\ln\left(\kappa^i + \lambda_0^i(\overline{\boldsymbol{\varepsilon}}^i)^2\right)+C_0}$$

$$\frac{1}{(1-d^i)} = \left(\kappa^i + \lambda_0^i(\overline{\boldsymbol{\varepsilon}}^i)^2\right)e^{C_0} = \left(\kappa^i + \lambda_0^i(\overline{\boldsymbol{\varepsilon}}^i)^2\right)C_i d^i = 1 - \frac{1}{\left(\kappa^i + \lambda_0^i(\overline{\boldsymbol{\varepsilon}}^i)^2\right)C_i} \tag{A.3}$$

Integration constant C_i can be obtained using the condition that damage potential must be equal to zero:

$$^{n+1}\Phi^i = \left(1 - {}^{n+1}d^i\right)\lambda_0^i{}^{n+1}\overline{\boldsymbol{\varepsilon}}^{i2} + \left(\kappa^i\left({}^nh^i + {}^nd^i - {}^{n+1}d^i\right) - \omega_0^i\right) = 0 \tag{A.4}$$

This gives integration constant, consequently damage variable as:

$$C = \frac{1}{\omega_0^i + \kappa^i}d^i = \frac{\lambda_0^i \varepsilon^{i2} - \omega_0^i}{\lambda_0^i \varepsilon^{i2} + \kappa^i} \tag{A.5}$$

The analytical solution for damage variable in A.6 makes the model fully defined analytically.

References

[1] Reid SR, Zhou G. Impact behaviour of fibre-reinforced composite materials and structures. Elsevier; 2000.

[2] Gholizadeh Samira. A review of impact behaviour in composite materials. Int J Mech Prod Eng 2019;7(3):28–39. IJMPE-IRAJ-DOIONLINE-15203 (in press).

[3] Ruiz C, Harding J. Modelling impact of composite structures using small specimens. Impact Behav Fibre-Reinforced Compos Mater Struct 2000:73–108.

[4] Wu E, Tsai C-Z. Impact behaviour and analysis of CFRP laminated plates. In: Reid SR, Zhou G, editors. Impact Behav. Fibre-Reinforced Compos. Mater. Struct., Woodhead Publishing Ltd. Cambridge, 2000: p. 212.

[5] Kim JK. Recent developments in impact damage assessment of fibre composites. Impact Behav. Fibre-Reinforced Compos. Mater. Struct. (2000) 33–74.

[6] Talreja R, Singh CV. Damage and failure of composite materials. Cambridge University Press; 2012.

[7] Schreyer HL. Continuum damage based on elastic projection operators. Int J Damage Mech 1995;4(2):171–95.

[8] Schreyer HL, Zuo QH. Anisotropic yield surfaces based on elastic projection operators. Trans ASME J Appl Mech 1995;62:780–5. https://doi.org/10.1115/1.2897014.

[9] Mehrabadi MM, Cowin SC. Eigentensors of linear anisotropic elastic materials. Q J Mech Appl Math 1990;43:15–41. https://doi.org/10.1093/qjmam/43.1.15.

[10] Mehrabadi MM, Cowin SC, Horgan CO. Strain energy density bounds for linear anisotropic elastic materials. J Elast 1993;30(2):191–6.

[11] Cowin SC, Mehrabadi MM. On the identification of material symmetry for anisotropic elastic materials. Q J Mech Appl Math 1987;40(4):451–76.

[12] Cowin SC, Mehrabadi MM. The structure of the linear anisotropic elastic symmetries. J Mech Phys Solids 1992;40:1459–71. https://doi.org/10.1016/0022-5096(92)90029-2.

[13] Hansen NR, Schreyer HL. A thermodynamically consistent framework for theories of elastoplasticity coupled with damage. Int J Solids Struct 1994;31(3):359–89.

[14] E-Xtream, Mesoscale composite model, (n.d.). https://www.e-xstream.com/products/digimat/about-digimat (accessed July 22, 2019).

[15] Gitman IM. Representative volume : Existence and size determination 2007;74:2518–34. https://doi.org/10.1016/j.engfracmech.2006.12.021.

[16] Ostoja-Starzewski M. Microstructural randomness versus representative volume element in thermomechanics. J Appl Mech 2002;69:25–35.

[17] LSTC, LS-Dyna Keyword User's Manual; Volume I: (R 7.1 edition), 2014.

[18] Millet JCF, et al. The effect of orientation on the shock response of a carbon fibre–epoxy composite. Compos Sci Technol 2007;67(15–16):3253–60.

[19] Millet JCF, et al. Response of a CFC to shock. Effects of orientation; 2007b.

[20] Hazell PJ. The dynamic behaviour of CFRP materials. ELRIPS 2007. WP6a-CU-TREP-07.

[21] Vignjevic R, Campbell JC, Bourne NK, Djordjevic N. Modeling shock waves in orthotropic elastic materials. J Appl Phys 2008;104(4):044904.

[22] Vignjevic R, Djordjevic N, Panov V. Modelling of dynamic behaviour of orthotropic metals including damage and failure. Int J Plast 2012;38:47–85.

[23] Liu J. Dyna3D: A nonlinear, explicit, three-dimensional finite element code for solid and structural mechanics. Livermore, (CA) USA: University of California, Lawrence Livermore National Laboratory; 2004.